atoms

MDPI

Article

Impact of Charge Migration and the Angle-Resolved Photoionization Time Delays of the Free and Confined Atom X@C_{60}

Subhasish Saha [1,2], Sourav Banerjee [3] and Jobin Jose [1,*]

[1] Department of Physics, Indian Institute of Technology Patna, Bihta 801103, Bihar, India; saha.154@osu.edu
[2] Department of Physics, The Ohio State University, Columbus, OH 43210, USA
[3] Center for Free-Electron Laser Science CFEL, Deutsches Elektronen-Synchrotron DESY, Notkestraße 85, 22607 Hamburg, Germany; sourav.banerjee@desy.de
* Correspondence: jobin.jose@iitp.ac.in

Abstract: The present study is devoted to isolate and study the effect of charge migration on the photoionization from the X@C_{60}. The noble gas atoms, Ar, Kr, and Xe, are confined in the C_{60} to investigate the impact of charge migration from the entrapped atom to the C_{60} side. The present work concludes that the confinement oscillations in the photoionization features are amplified due to the charge migration. Further, the angle-resolved, spin average time delay is also investigated in the light of confinement. Features in the time delay due to the charge migration are more amplified relative to those in the cross-section or angular distribution.

Keywords: photoionization; confined atom; GASW potential; charge migration; time delay

Citation: Saha, S.; Banerjee, S.; Jose, J. Impact of Charge Migration and the Angle-Resolved Photoionization Time Delays of the Free and Confined Atom X@C_{60}. *Atoms* **2022**, *10*, 44. https://doi.org/10.3390/atoms10020044

Academic Editor: Eugene T. Kennedy

Received: 31 March 2022
Accepted: 28 April 2022
Published: 30 April 2022

1. Introduction

The study of photoionization from atoms entrapped in fullerene molecules allows us to understand that the dynamical properties of atoms and molecules undergo a drastic change when they are spatially confined in either a penetrable or an impenetrable cavity as compared to their free counterparts [1,2]. These changes are primarily due to the alterations in the electronic structure properties of X@, such as binding energy, electronic probability distribution, correlation, and relativistic effects [3–5]. In addition, the photoelectron interacts with the confinement cage, leading to features such as confinement oscillations [6], Coulomb-confinement resonances [7], and interchannel coupling effects of photoionization channels from the C_{60} and the entrapped atom [8,9]. For example, a huge enhancement in the cross-section is observed due to the coupling of the atomic photoionization channels with the giant plasmon resonance of the surrounding fullerene. Owing to the aforementioned importance of confined system, the structural and dynamical properties of X@C_{60} have been investigated by employing several single-active-electron approximation and many-electron techniques [10–17].

Although the electromagnetic radiation interacts with the confined system as a whole, it is extremely interesting to decouple the effects of C_{60} and the atom in the whole photoionization process. This is possible by secluding the channels from the X@ and those from the C_{60} itself. So far, the most sophisticated calculation of X@C_{60} has been performed by employing the time-dependent local density approximation (TDLDA) by Himadri et al., which includes the coupling effects of channels from the C_{60} and the X@ [18]. The TDLDA treats all the valence electrons, four ($2s^2 2p^2$) from each carbon atom in the fullerene, to form the delocalized charged cloud. The residual ion core composed of all C^{4+} ions is treated by a classical jellium shell. While looking for the realistic nature of the confining potential, a method that explicitly includes the position of each C atom of the C_{60} with the correct icosahedral (I_h) symmetry is an ideal choice. Nevertheless, considering the high symmetry

of the $C_{60,}$ a spherically averaged jellium model potential is also ideal to describe that all the valence electrons form a delocalized charged cloud with the residual ion core composed of all C^{4+} ions. Thus, the spatial distribution of the positive charge of the C nuclei and negative charge distribution of the electrons of C_{60} is realistically represented by a jellium potential with diffuse but compact borders [8,9,19]. The entrapped atom is placed at the center of the C_{60} shell, and the Kohn–Sham equations for the (240 + N)-electron system (240 cage electrons and N = number of electrons of the entrapped atoms) are then solved to obtain the ground-state wave function of the system in the local-density approximation (LDA). Hence, the inclusion of the realistic effects of C_{60} confinement can be considered more appropriate. One may be reminded that the potential employed in the works of Puska and Nieminen [19] is also a similar one, and the Gaussian annular square well (GASW) potential [20] is a parametric representation of the realistic potential derived from the LDA, used in the TDLDA works by Himadri et al. [8].

One of the realistic effects of confinement predicted in the works of Himadri et al. [9] is the hybridization of atomic orbitals with that of the C_{60}; the effects are seen in He@C_{60}, Ne@C_{60}, Ar@C_{60}, Kr@C_{60}, Xe@C_{60}, Ba@C_{60}, and Mg@C_{60} [2,9,21]. Recently, a work by Shields et al. [22] contrasted the hybridization properties of Ar@C_{60} and Cl^{-}@C_{60} and the impact on the photoionization from these hybrid systems. It has been argued in the works of Javani et al. using the LDA [9] that the hybridization adds to the confinement oscillations of the cross-section. For example, the powerful hybridization of the Xe 5*s* state with the C_{60} π orbital induces strong oscillatory structures in the 5*s* ionization cross-section. The work also included the impact of coupling with photoionization channels from the C_{60}. In the region of giant plasmon resonances, 16.5 eV and 38 eV [18], the cross-section is amplified many times due to the coupling of channels from X@ and C_{60}. For instance, the hybridization effect on the Xe 5*p* cross-section is greatly enhanced by borrowing considerable oscillator strength from the C_{60} giant plasmon resonance via the atom–fullerene dynamical interchannel coupling. However, the isolated impact of hybridization on photoionization was not accounted for in their study.

From the above discussion, it is clear that the enhancement in cross-section is due to two factors: (i) hybridization and (ii) coupling of photoionization channels with C_{60} electrons. The objective of the present work is to (i) decouple the effects and (ii) to see to what degree the hybridization affects the photoionization dynamics. For this purpose, we have employed the GASW model potential [20] in the RRPA methodology to obtain the photoionization parameters. Indeed, a model potential approach using GASW cannot mimic the hybridization properties since there is no possibility of the mixing of the atomic wavefunctions with that of the cage (C_{60}) due to the lack of a realistic representation of the C_{60} electrons. Nevertheless, by tuning the confinement well depth of the model potentials, one can see the transfer of electron from the atomic side to the well side. This transfer of the electronic cloud of confined atoms to the C_{60} side with the variation of the depth of the static model potential is denoted as *charge migration* hence forth. Although this is not a hybridization in a realistic sense, one may expect to obtain an electronic density distribution similar to that of the hybridization using the model potential approach. Therefore, the present approach is to generate an identical electron density as in the case of hybridization and then to study the photoionization parameters of the charge-migrated system. In this way, we seclude the channels from the C_{60} so that the impact of charge transfer alone on the photoionization parameters can be investigated.

The work draws a close connection with the photoionization studies of Madjet et al. [18,23] for two reasons: (1) The confinement environment employed (GASW) is just a parametric representation of their potential, and (2) the GASW depth is tuned such that the altered electronic density is akin to that used in the TDLDA calculations. Because of the second reason, to a good approximation, it is assumed that the photoionization is taking place from the hybridized orbital of the trapped atom. In the present work, the main focus is to see how the effect of charge migration propagates along the series of the various noble gas atoms (Ar, Kr, and Xe) entrapped in C_{60}. The photoionization cross-section of the charge-migrated X@

is compared with published results that include the effect of the coupling of photoionization channels with C_{60} orbitals. In this paper, we also investigate the effect of charge migration on the photoelectron asymmetry parameter and the angle-dependent, spin-averaged time delay using the dipole relativistic random phase approximation (RRPA) by including the full interference of all the relevant spin–orbit-coupled photoionization channels.

The success of RRPA in dealing with the photoionization process is well known. For instance, the earlier results on photoionization based on the RRPA formalism have been compared with experiments in many previous studies and are in good agreement [24–26]. Furthermore, the accuracy of RRPA results in calculating the photoionization from the confined atom is also quite superior, which is evident from the agreement between the theory and experiment [24,27,28]. The time delay in the atomic photoionization is yet another concept that is amenable to experimental verification. The time delay in atomic processes was first introduced by Wigner [29], and is well defined in terms of energy derivative of the phase shift of the outgoing photoelectron wavepacket. The RRPA has been extensively used in predicting the photoionization time delay from atoms and confined atoms [30,31]. Due to the anisotropy of the photoionization process, the dipole transition amplitude is written as the linear superposition of the relativistic dipole terms associated with spherical harmonics, which leads to angle-dependent time delay. Very limited results on time delay are available from experiments [32,33], whereas the cross-section and beta values are verified with the experimental values [34]. The angular time delay being a nascent and emerging field, experimental verification of it is much awaited.

In Section 2, a brief discussion of the calculational methodology is presented, and Section 3 discusses the results and the observations, which are concluded in Section 4.

2. Theoretical Methodology

The present work uses the multichannel RRPA formalism of Johnson and Lin [12,35] for simulating the photoionization process from confined atoms. In this formalism, the transition amplitude is caused by the electromagnetic interaction, which is treated as a perturbation $\nu_+ = e\vec{\alpha}.\vec{A}$, $\nu_- = \nu_+^\dagger$. The transition probability amplitude (T) is defined as

$$T = \sum_{i=1}^{N} e \int d^3r \left(\omega_{i+}^\dagger \left(\vec{\alpha}.\vec{A} \right) u_i + \omega_{i-}^\dagger \left(\vec{\alpha}.\vec{A} \right)^\dagger u_i \right), \tag{1}$$

where u_i and $\omega_{i\pm}$ are the respective ground and excited states of the electron of confined atom and $\vec{A}$ is the vector potential.

The RRPA includes many-electron correlation effects in both initial states and final states through the time dependence in $\vec{A}$ in the above equation; all possible two-electron, two-hole excitations are accounted for in the initial state and interchannel coupling of the final-state channels, which amounts to continuum configuration interaction. In the RRPA [12,13,25,35], the interchannel coupling effect refers to the interference effect of different continuum channels mediated via the positive and negative frequency terms in Equation (1).

The multipole transition amplitude for an electronic excitation from an initial state, $a = n\kappa$, to a final energy scale normalized state, $\bar{a} = E\bar{\kappa}$, is given in the RRPA by [12]

$$\begin{aligned} T_{JM}^{(\lambda)} &= \int d^3\vec{r}\, \vec{\omega}_i^\dagger . \vec{\alpha} . \vec{a}_{JM}^{(\lambda)} u_i \\ &= i\left(\frac{2\pi^2}{EP}\right)^{1/2} \left(\frac{(2J+1)(J+1)}{J}\right)^{1/2} \frac{\omega^J}{(2J+1)!!} \sum_{\vec{\kappa}\,\vec{m}} \chi_\nu^\dagger \Omega_{\bar{\kappa}\bar{m}}(\hat{p})\, (-1)^{\bar{j}-\bar{m}} \begin{pmatrix} \bar{j} J j \\ -\bar{m} M m \end{pmatrix} \\ &\times i^{1-\bar{l}} e^{i\delta_{\bar{\kappa}}} \left\langle \bar{a} \| Q_J^{(\lambda)} \| a \right\rangle_{RRPA}. \end{aligned} \tag{2}$$

Here, $\bar{\kappa} = \mp(\bar{j} + \frac{1}{2})$ for $\bar{j} = (\bar{l} \pm \frac{1}{2})$, J is the angular momentum quantum number of the photon, and M is its projection. The parameter λ takes the value 1 or 0 depending upon

the electric or magnetic case. The $\delta_{\overline{\kappa}}$ is the complex dipole phase of the transition, and $\left\langle \overline{a}\|Q_J^{(\lambda)}\|\, a\right\rangle_{RRPA}$ is the reduced matrix element associated with electric dipole transition. The expression of $\left\langle \overline{a}\|Q_J^{(\lambda)}\|\, a\right\rangle_{RRPA}$ is taken from Refs. [12,30]. The spherical spinor is given in terms of the Clebsch–Gordon coefficients, the spherical harmonics, and two-component Pauli spinors χ_v as

$$\Omega_{\kappa m}(\hat{n}) = \sum_{\nu=\pm 1/2} C^{\bar{j}\overline{m}}_{\bar{l}\overline{m}-\nu,1/2\nu} Y_{\bar{l}m-\nu}(\hat{k})\chi_v \tag{3}$$

Here, $\nu = \pm\frac{1}{2}$ is the spin polarization of the photoelectron.

Since we are dealing with electric dipole photoionizing transitions, we set $\lambda = 1, J = 1$ and choose $M = 0$, which corresponds to the linear polarization in the z-direction. In this case, the amplitude for a relativistic electric dipole transition (Equation (2)) is reduced to [36]

$$\begin{aligned}[T^{1v}]^m_{nlj} = &\sum_{\overline{\kappa}\overline{m}} C^{\bar{j}\overline{m}}_{\bar{l}\overline{m}-\nu,1/2\nu} Y_{\bar{l}\overline{m}-v}(\hat{\kappa})(-1)^{2\bar{j}+j+1-\overline{m}} \\ &\times \begin{pmatrix} \bar{j} & 1 & j \\ -\overline{m} & 0 & m \end{pmatrix} i^{1-\bar{l}} e^{i\delta_{\overline{\kappa}}} \left\langle \overline{a}\right| \left| Q_1^{(1)} \right| \left| a\right\rangle_{RRPA}\end{aligned} \tag{4}$$

One can obtain the dipole matrix element in terms of a reduced matrix element modified by a phase factor for a particular transition between the initial state $j = a$ and final state $\bar{j} = \overline{a}$ as

$$D_{j\to\bar{j}} = i^{1-\bar{l}} e^{i\delta_{\overline{\kappa}}} \left\langle \overline{a}\|Q_1^{(1)}\|\, a\right\rangle_{RRPA} \tag{5}$$

The total dipole photoionization cross-section is given by

$$\sigma_{n\overline{\kappa}}(\omega) = \frac{4\pi^2\alpha\omega}{3}\left(\left|D_{j\to j-1}\right|^2 + \left|D_{j\to j}\right|^2 + \left|D_{j\to j+1}\right|^2\right). \tag{6}$$

The dipole angular distribution asymmetry parameter β is written in terms of dipole matrix elements as

$$\begin{aligned}\beta_{n\kappa}(\omega) = &\left\{ \begin{array}{l} \frac{(2j-3)}{2(2j)}\left|D_{j\to j-1}\right|^2 - \frac{(2j-1)(2j+3)}{2(2j+2)}\left|D_{j\to j}\right|^2 \\ +\frac{(2j+5)}{2(2j+2)}\left|D_{j\to j+1}\right|^2 - \frac{3}{2j}\left(\frac{(2j-1)}{2(2j+2)}\right)^{1/2}\left(D_{j\to j-1}D^*_{j\to j} + c.c\right) \\ -\frac{3}{2}\left(\frac{(2j-1)(2j+3)}{2j(2j+2)}\right)^{1/2}\left(D_{j\to j-1}D^*_{j\to j+1} + c.c\right) \\ +\frac{3}{(2j+2)}\left(\frac{(2j+3)}{2(2j)}\right)^{1/2}\left(D_{j\to j}D^*_{j\to j+1} + c.c\right) \end{array} \right\} \\ &\times\left\{\left|D_{j\to j-1}\right|^2 + \left|D_{j\to j}\right|^2 + \left|D_{j\to j+1}\right|^2\right\}^{-1}\end{aligned} \tag{7}$$

Note that the term $D_{j\to j-1}$ in Equations (6) and (7) is absent for $j = 1/2$. In Equation (6), α is the fine structure constant and ω is the photon energy.

An electric dipole transition originating from ns and np initial states leads to the following seven relativistic ionization channels:

$$\begin{aligned} np_{1/2} &\to \varepsilon s_{1/2}, \varepsilon d_{3/2} \\ np_{3/2} &\to \varepsilon s_{1/2}, \varepsilon d_{3/2}, \varepsilon d_{5/2} \\ ns_{1/2} &\to \varepsilon p_{1/2}, \varepsilon p_{3/2} \end{aligned}$$

The dipole channels are coupled in the RRPA calculation for each of the atoms so that the correlation effects in the final state are accounted for to the extent possible.

In the RRPA, the values of $\sigma_{np_{1/2}}, \beta_{np_{1/2}}$ and $\sigma_{np_{3/2}}, \beta_{np_{3/2}}$ are calculated, and then the total cross-section and angular asymmetry parameters for an np subshell are written as [35]

$$\sigma_{np} = \sigma_{np_{1/2}} + \sigma_{np_{3/2}} \tag{8}$$

$$\beta_{np} = \frac{\beta_{np_{1/2}}\sigma_{np_{1/2}} + \beta_{np_{3/2}}\sigma_{np_{3/2}}}{\sigma_{np_{1/2}} + \sigma_{np_{3/2}}} \tag{9}$$

Using Equation (4), one can easily derive the relativistic ionization amplitudes for *ns* and *np* initial states [25].

$$[T_{10}^{1+}]_{ns_{1/2}}^{m=1/2} = -\frac{1}{3\sqrt{2}}Y_{10}D_{ns_{1/2}\to Ep_{1/2}} - \frac{1}{3}Y_{10}D_{ns_{1/2}\to Ep_{3/2}}; \tag{10a}$$

$$[T_{10}^{1-}]_{ns_{1/2}}^{m=1/2} = \frac{1}{3}Y_{11}D_{ns_{1/2}\to Ep_{1/2}} - \frac{1}{3\sqrt{2}}Y_{11}D_{ns_{1/2}\to Ep_{3/2}}; \tag{10b}$$

$$[T_{10}^{1+}]_{np_{1/2}}^{m=1/2} = +\frac{1}{\sqrt{15}}Y_{20}D_{np_{1/2}\to Ed_{3/2}} + \frac{1}{\sqrt{6}}Y_{00}D_{np_{1/2}\to Es_{1/2}}; \tag{10c}$$

$$[T_{10}^{1-}]_{np_{1/2}}^{m=1/2} = -\frac{1}{\sqrt{10}}Y_{21}D_{np_{1/2}\to Ed_{3/2}}; \tag{10d}$$

$$\begin{aligned}[T_{10}^{1+}]_{np_{3/2}}^{m=1/2} = {} & \tfrac{1}{\sqrt{6}}Y_{00}D_{np_{3/2}\to Es_{1/2}} - \tfrac{1}{5\sqrt{6}}Y_{20}D_{np_{3/2}\to Ed_{3/2}} \\ & -\tfrac{1}{5}\sqrt{\tfrac{3}{2}}Y_{20}D_{np_{3/2}\to Ed_{5/2}};\end{aligned} \tag{10e}$$

$$[T_{10}^{1-}]_{np_{3/2}}^{m=1/2} = \frac{1}{10}Y_{21}D_{np_{3/2}\to Ed_{3/2}} - \frac{1}{5}Y_{21}D_{np_{3/2}\to Ed_{5/2}}; \tag{10f}$$

$$[T_{10}^{1+}]_{np_{3/2}}^{m=3/2} = -\frac{3}{\sqrt{10}}Y_{21}D_{np_{3/2}\to Ed_{3/2}} - \frac{2\sqrt{3}}{15}Y_{21}D_{np_{3/2}\to Ed_{5/2}}; \tag{10g}$$

$$[T_{10}^{1-}]_{np_{3/2}}^{m=3/2} = \frac{3}{\sqrt{5}}Y_{22}D_{np_{3/2}\to Ed_{3/2}} - \frac{\sqrt{3}}{15}Y_{22}D_{np_{3/2}\to Ed_{5/2}} \tag{10h}$$

The amplitudes corresponding to m = +1/2 are only considered in Equation (4), and the amplitudes associated with m = −1/2 will have just a similar structure due to symmetric inversion of spin projection of m = +1/2 about the polarization axis (z-direction) of the photon. Because of the anisotropy of the photoionization process, the time delay is angle-dependent. The spherical spinor in the expression of transition amplitude (Equation (2)) contains the angle information in spherical harmonics Y_{lm}. The interference between two different quantum paths, which lead to two different final state continua of different symmetry from the same initial bound state, makes the time delay angle sensitive. However, the Wigner time delay associated with each amplitude is given by

$$\tau = \frac{d\eta}{dE}, \eta = \tan^{-1}\left[\frac{\mathrm{Im}T_{10}^{1\pm}}{\mathrm{Re}T_{10}^{1\pm}}\right] \tag{11}$$

The spin-averaged time delay for $ns_{1/2}$ state can be expressed as

$$\overline{\tau}_{ns_{1/2}} = \frac{\tau_{ns_{1/2}}^{m=1/2,+}\left|[T_{10}^{1+}]_{ns_{1/2}}^{m=1/2}\right|^2 + \tau_{ns_{1/2}}^{m=1/2,-}\left|[T_{10}^{1-}]_{ns_{1/2}}^{m=1/2}\right|^2}{\left|[T_{10}^{1+}]_{ns_{1/2}}^{m=1/2}\right|^2 + \left|[T_{10}^{1-}]_{ns_{1/2}}^{m=1/2}\right|^2} \tag{12}$$

The spin-averaged time delay for $np_{1/2}$ state becomes

$$\overline{\tau}_{np_{1/2}} = \frac{\tau_{np_{1/2}}^{m=1/2,+}\left|[T_{10}^{1+}]_{np_{1/2}}^{m=1/2}\right|^2 + \tau_{np_{1/2}}^{m=1/2,-}\left|[T_{10}^{1-}]_{np_{1/2}}^{m=1/2}\right|^2}{\left|[T_{10}^{1+}]_{np_{1/2}}^{m=1/2}\right|^2 + \left|[T_{10}^{1-}]_{np_{1/2}}^{m=1/2}\right|^2} \tag{13}$$

The spin-averaged time delay for $np_{3/2}$ state becomes

$$\overline{\tau}_{np_{3/2}} = \frac{\begin{array}{c}\tau^{m=1/2,+}_{np_{3/2}}\left|\left[T^{1+}_{10}\right]^{m=1/2}_{np_{3/2}}\right|^2 + \tau^{m=1/2,-}_{np_{3/2}}\left|\left[T^{1-}_{10}\right]^{m=1/2}_{np_{3/2}}\right|^2 \\ +\tau^{m=3/2,+}_{np_{3/2}}\left|\left[T^{1+}_{10}\right]^{m=3/2}_{np_{3/2}}\right|^2 + \tau^{m=3/2,-}_{np_{3/2}}\left|\left[T^{1-}_{10}\right]^{m=3/2}_{np_{3/2}}\right|^2\end{array}}{\begin{array}{c}\left|\left[T^{1+}_{10}\right]^{m=1/2}_{np_{3/2}}\right|^2 + \left|\left[T^{1-}_{10}\right]^{m=1/2}_{np_{3/2}}\right|^2 \\ +\left|\left[T^{1+}_{10}\right]^{m=3/2}_{np_{3/2}}\right|^2 + \left|\left[T^{1-}_{10}\right]^{m=3/2}_{np_{3/2}}\right|^2\end{array}} \tag{14}$$

Coming to the confinement, conventionally, the depth of the model potential is calibrated by reproducing the known electron affinity of the C_{60}, giving a semiempirical qualification of the model potential [37,38]. For the C_{60} fullerene, the depth of the annular square well (*ASW*) potential ($V_{ASW}(r)$) is modeled such that the electron trapped in the well has binding energy identical to that of real fullerene, and its value is accepted to be −0.422 a.u. [5,39]. However, there are other values also under consideration for V_{ASW}. In the works of Connerade et al. [40] and Varma et al. [41], the V_{ASW} is taken as −0.302 a.u., while that in the work of Winstead and Mckoy [42] and Dolmatov et al. [43] is taken as approximately −0.26 a.u. On the other hand, in the present work, we choose the strength of the potential by altering the depth to get an identical electronic density distribution as that from a more realistic (LDA) calculation [8,9,18,23]. To have a hand-in-hand consistency with the works by Madjet et al. [18,23], we choose the GASW potential for the model confinement. The $V_{GASW}(r_c)$ is given as

$$V_{GASW}(r) = \frac{D}{\sqrt{2\pi}\sigma} e^{-\left(\frac{r-r_c}{\sqrt{2}\sigma}\right)^2} + V_{ASW}(r), \tag{15}$$

where $D = -3.59$ a.u., standard deviation $\sigma = 1.70$ a.u., radius $r_c = 6.7$ a.u., and thickness $\Delta = 2.8$ a.u. and the ASW model potential is written as

$$V_{ASW}(r) = \begin{cases} -U, \; r_c - \frac{\Delta}{2} \leq r \leq r_c + \frac{\Delta}{2} \\ 0\,, \text{ otherwise} \end{cases} \tag{16}$$

where U is the depth of the potential. Details of the GASW model potential can be found elsewhere [20,44]. The DF equations are solved for the entrapped noble gas elements, Ar@, Kr@, and Xe@, to obtain the altered electronic density. The depth of the GASW potential adopted for the entrapped atoms to have almost identical charge density as that of the LDA calculations is 1.8 a.u. for Ar *3p*, 1.8 a.u. for Kr *4p*, and 2.2 a.u. for Xe *5s* and *5p*.

The RRPA calculations are performed to investigate the impact of charge transfer on the photoionization parameters. To accomplish the aim, three levels of calculations are performed for an atom@, using (i) depth = 0, corresponding to the free atom, (ii) depth ~0.3 a.u., which is the conventional depth for the potential in the works of Varma et al. [41] and Connerade et al. [40], and (iii) the particular depth at which the atom@ electron density is akin to the LDA calculation. A comparison of the results from these three levels of calculation enables us to identify the impact of charge transfer/hybridization on photoionization.

3. Results and Discussion

The RRPA calculations are performed with the following coupled channels:

(a) 16 channels for Ar (all the dipole channels from 3p, 3s, 2p, 2s, and 1s are coupled);
(b) 20 dipole channels from Kr (channels from the 4p, 4s, 3d, 3p subshells are coupled);
(c) 20 dipole channels for Xe (channels from 5p, 4d, 5s, 4p, and 4s subshells are coupled).

The comparison of the charge migration results with LDA and TDLDA [9,18,23] results provides a better understanding of the importance of hybridization. The subsections are organized in the order Ar@C_{60}, Kr@C_{60}, and Xe@C_{60}.

Ar@C_{60}

Figure 1 shows the $3p_{1/2}$ radial wavefunction of free and confined Ar, with two different confinement depths, 0.3 a.u. and 1.8 a.u. Table 1 shows the corresponding binding energies for the $3p_{1/2}$ and the $3p_{3/2}$ subshells obtained in the DF formalism. Since the Ar is less relativistic, the spin–orbit split subshells exhibit identical behavior and hence only the $3p_{1/2}$ wavefunction is shown in Figure 1. The wavefunction of Ar@C_{60} $3p$ subshell exhibits free atom-like behavior in the case of confinement depth $V_{GASW}(r_c)$ = 0.3 a.u. However, one may note that the binding energies of the spin–orbit split subshells are different for these two cases, as evident from Table 1. This means that except for the binding energy change, the confinement with depth $V_{GASW}(r_c)$ = 0.3 a.u. is not sufficient to alter the electronic charge densities of Ar@. When the confinement depth $V_{GASW}(r_c)$ = 1.8 a.u, the $3p$ wave function exhibits a mixed character of the atomic state and the well state. This is accomplished via the charge transfer of densities from the atomic side to the well side. The $3p$ wavefunction of the Ar@ is expressible as a linear combination of the Ar and the well state. Moreover, the binding energies are also enhanced owing to the increased confinement potential (Table 1). Figure 1 also facilitates a comparison of the electronic density with that from the LDA calculations. At the depth = 1.8 a.u, the $3p$ wavefunction is in good agreement with the ab initio LDA theory [9]. Nevertheless, there is a shift in the thresholds in both LDA and the DF calculations. The difference in the binding energies does not pose a serious difficulty to continue, since the difference is expected to merely shift the onset of the cross-section [45,46]; however, the initial charge density affects the dynamics properties decisively. Since the relativistic effects are less dominant, the $3p_{3/2}$ and $3p_{1/2}$ wavefunctions are exactly similar in the case of $V_{GASW}(r_c)$ = 1.8 a.u. The charge-migrated $3p$ wavefunction exhibits an extra node in the vicinity of the cage. It is well known that the C_{60} orbitals are commonly classified as π or σ orbital depending on whether the orbital has a node in the center of the cage or not. This means that the well state of Ar@C_{60} in our calculation corresponds to a π orbital of the C_{60}. In other words, if the charge-migrated state is akin to a hybridized orbital, then the C_{60} orbital would correspond to a π state. This is supportive of the reported observation in the density functional theory studies of Ar@C_{60} that the Ar $3p$ orbital is hybridized with a C_{60} π function, leading to a node in the electronic density within the shell region [9]. Next, we attempt to see the contrast between photoionization parameters of free and confined cases of Ar with $V_{GASW}(r_c)$ = 0.3 a.u. and $V_{GASW}(r_c)$ = 1.8 a.u.

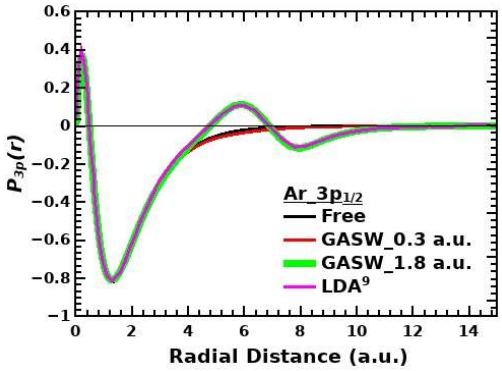

Figure 1. The large component of $3p_{1/2}$ radial wavefunction of free and confined Ar.

Table 1. 3*p* subshell thresholds of free and confined Ar.

Depth (a.u.)	Subshells	RRPA (eV)
0 (Free)	3p3/2	15.994
	3p1/2	16.198
0.3	3p3/2	16.432
	3p1/2	16.64
1.8	3p3/2	18.129
	3p1/2	18.323

The results for the cross-sections of *3p* subshell (using Equation (8)) for both free and confined Ar are shown in Figure 2, which are also compared with the existing LDA and TDLA results. It may be noted that the LDA results do not take into account the interchannel coupling effects, giving an uncorrelated picture, whereas the TDLDA does include the coupling effects. In Figure 2a, the photoionization cross-sections from the 3p orbital of free and confined Ar using the RRPA are compared with LDA results [23]. The *3p* cross-section for the free and the Ar@C_{60} with depth = 0.3 a.u. using the RRPA exhibits almost identical features except for the mild confinement oscillations in the latter. The Cooper minimum is almost unaffected because of the mild confinement, which induced no charge migration. The scenario is drastically modified for the Ar@C_{60} with the confinement depth of $V_{GASW}(r_c)$ = 1.8 a.u., where the cross-section in the RRPA is modulated severely by the confinement oscillations. Destructive interference in the photon energy at 24 eV has brought down the cross-section magnitude at this depth. Moreover, the Cooper minimum, which was at 50 eV earlier is pushed by a few electron-volt (eV) in the charge-migrated case. One may conclude from these observations that the charge migration is responsible for these changes. The cross-sections obtained from the LDA show huge differences from the other results; it is nearly an order of magnitude larger than other results at the threshold. Note that the LDA results do include the effect of hybridization, but it is done in an independent particle approximation. Thus, the final state correlation effects due to the interchannel coupling are taken into account in the RRPA calculation, which is left out in the LDA calculation. This disparity in the inclusion of correlation effects makes the discrepancy between the LDA and the RRPA results.

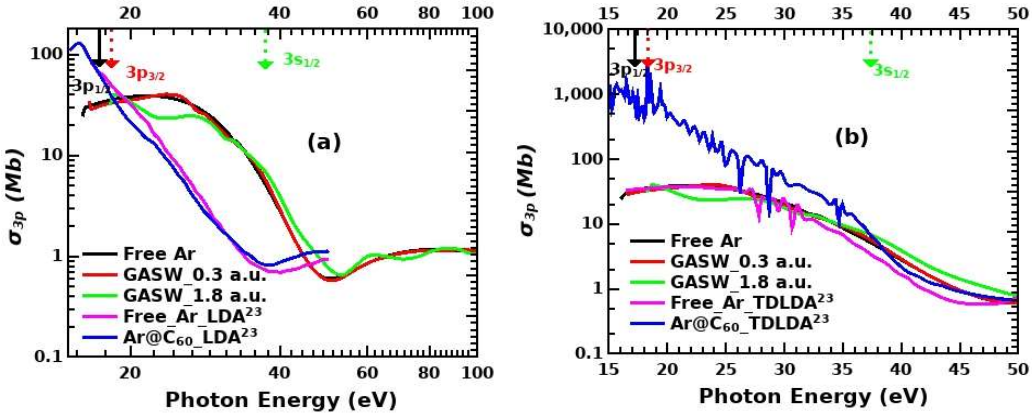

Figure 2. The RRPA photoionization cross-section of the 3p orbital of free and confined Ar is compared with (**a**) LDA [23] and (**b**) TDLDA [23] results. Vertical arrows indicate the threshold values of the corresponding subshells used in the RRPA.

In Figure 2b, the photoionization cross-sections from the 3p orbital of free and confined Ar are compared with the TDLDA results [23]. For the free atom, although the LDA overestimates the cross-section near the threshold, the result from the TDLDA calculation agrees with the RRPA cross-section. This is because both the methodologies take into account the correlation effects to a similar extent, and therefore these methods are on an

equal footing. However, for confined Ar, the cross-section in the TDLDA is enhanced almost by two orders of magnitude at the threshold. This enhancement is [23] due to two factors: first, the hybridization of Ar orbital, and the second one is owing to the coupling of photoionization channels with C_{60} electron. As mentioned earlier, in the TDLDA, it was not possible to decouple both the effects to see their individual contributions; the current model potential approach with the RRPA does enable to perceive the decoupled effect. We observe that the impact of the charge migration is to enhance the confinement oscillation about the free atom 3p cross-section. In other words, the enhancement in low-energy cross-section in the TDLDA predominantly arises due to the coupling of photoionization channels with the C_{60} electron.

The foregoing discussion confirmed that the impact of charge migration is to enhance the confinement oscillations; an explanation for this behavior is given here. In low-depth cases, the ejected photoelectron comes out only from the atomic side and bounces off the walls of C_{60}, which further interferes with the photoelectron, leading to ordinary confinement oscillations. However, in the charge-migrated case, confinement resonances are stronger. There are additional interference pathways in the charge-migrated case. For instance, probabilistically, the photoelectron can come out from the atomic side and the well side depending on the level of the charge migration. In other words, the continuum wavefunction is expressible as a linear superposition of that of both the channels. Consequently, the interference can happen when the (1) photoelectron comes from the atomic side and is reflected from the inner and outer walls of the C_{60} and the (2) photoelectron comes from the well side and is bounced from the inner and outer walls of the C_{60}. The interference between (1) and (2) leads to additional confinement oscillations. One may also interpret it from a configuration interaction (CI) perspective. For the confinement depth $V_{GASW}(r_c)$ = 1.8 a.u., the Ar@ wavefunction can be written as a linear combination of atomic state and the well state: $\Psi_{Ar@C_{60}} = c_1\psi_{Ar} + c_2\psi_{C_{60}}$, just akin to a multiconfiguration initial state. It is well known that a state approximated by the linear superposition of configurations does support more channels compared to the single configuration case [47]. The coupling of these additional channels will lead to enhanced interference, resulting in larger confinement oscillations in the present case.

In Figure 3, we show the average angular asymmetric parameter β_{3p} of free and Ar@C_{60}, calculated by the RRPA using Equation (9). The β_{3p} shows almost identical features for the free Ar and Ar@C_{60} with $V_{GASW}(r_c)$ = 0.3 a.u.; it increases to a maximum value at 40 eV and displays a minimum at 50 eV. Note that the minimum in the β_{3p} happens at the location of the Cooper minimum. Nevertheless, a feeble confinement oscillation can be seen over the free parameter. This shows that the low-depth confinement does not alter the angular distribution compared to that of the free Ar. However, the situation is different for the Ar@C_{60} with depth = 1.8 a.u., where the confinement oscillation dramatically modifies the β_{3p} compared to that of the free atom. At the cooper minimum location, the β_{3p} attains a lower value compared to other cases. This is the impact of confinement oscillations. After the Cooper minimum point, enhanced confinement resonance is observed for the depth of 1.8 a.u.

One may incidentally note that the impact of the charge migration is comparatively severe in the angular distribution compared to that on the cross-section. This is because the β contains the relative phase information of dipole channels, which is not the case in cross-section; see Equations (5) and (7) for details. The dipole amplitude, thus, is written as $D = |D|e^{i\phi}$; |D| is the dipole amplitude and ϕ is relative phase. The ϕ is extremely sensitive to the confinement environment as the outgoing photoelectron gathers extra phase shift when it scatters with the confinement walls. This is in addition to the phase shift due to the electron–electron short-range interactions. The GASW provides rather a continuous variation of the confinement potential, which results in a smoother development of the phase shift with respect to the radial distance, resulting in larger values in the asymptotic regions. This point is confirmed in our SAE approximation calculations in Refs. [20,44], presented as a comparison between the ASW and the GASW scattering phase shifts. From

this perspective, one can expect the time delay in photoionization is also sensitive to the charge migration, which is analyzed next.

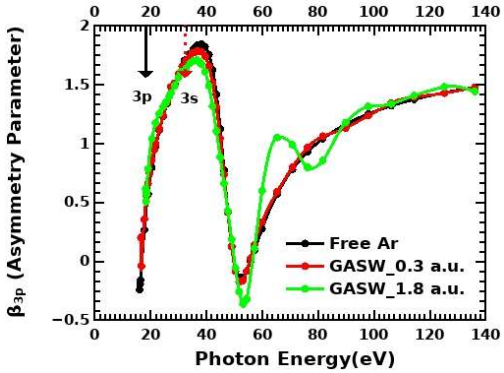

Figure 3. The average angular asymmetric parameter β_{3p} of free and Ar@C_{60}. Vertical arrows indicate the threshold values of the corresponding subshells used in the RRPA.

Figure 4 shows the individual channel time delay corresponding to 3p of free and confined Ar; the left panel corresponds to the free Ar, and the middle and the right panels are respectively for the Ar@C_{60} with depths 0.3 a.u. and 1.8 a.u. Left and right axis scales in each panel respectively correspond to p→εd and p→εs transition channels. Cooper minima corresponding to a p subshell are exhibited as a π jump in the phase shift, which results in a sharp and deeper negative time delay at 50 eV in the p→εd channel. Since the p→εs channel does not have the Cooper minimum, the rapid jump in phase shift and the time delay are missing. The average 3p time delays are also shown in Figure 4; this is defined as the sum of the $3p_j$ time delays weighted by the ratio of the respective individual channel cross-sections to the total of the cross-sections. The average $3p$ time delay is wider and less shallow compared to $3p \rightarrow \varepsilon d$ individual time delays in the region of Cooper minima due to the contribution from the $3p \rightarrow \varepsilon s$ channels. Except at the location of the Cooper minimum, the average time delay is similar to that of the $3p \rightarrow \varepsilon d$ channel due to the dominance of it. Unlike in the case of cross-section and angular distribution, the time delay exhibits larger confinement oscillations even for the low-depth confined case (middle panel). This is anticipated as the phase shift exhibits a larger sensitivity to the confinement than the absolute dipole matrix element does. For the $V_{GASW}(r_c)$ = 1.8 a.u., the confinement oscillations are enhanced due to charge migration. In this case, the confinement oscillations are even more dramatic in the time delay than in the cross-section or angular distribution asymmetry parameter.

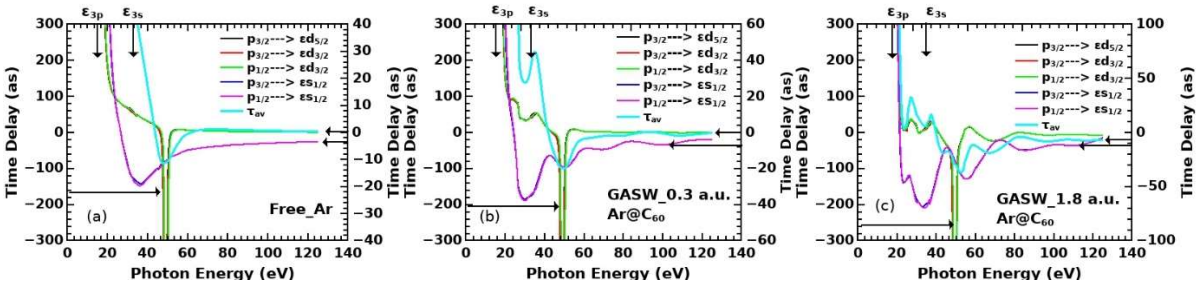

Figure 4. Time delay of photoionization from the 3p subshells of (**a**) free (**left panel**) and confined Ar with the depths of (**b**) 0.3 a.u. (**middle panel**) and (**c**) 1.8 a.u. (**right panel**). Left and right axes are the time scale of the p→εd and p→εs channels, respectively, which are indicated by the horizontal arrows. The average time delay $(\tau_{av})_{3p}$ is also linked to the right axis. Vertical arrows indicate the threshold values of the corresponding subshells used in the RRPA.

Figure 5 shows the spin-averaged, angle-dependent time delay of the photoionization from the $3p_{1/2}$ and the $3p_{3/2}$ subshells of Ar. The time delay of the $3p_{1/2}$ and $3p_{3/2}$ subshells is very similar, indicating that the spin–orbit interaction is not important here. Figure 5 shows that the time delay in the vicinity of Cooper minimum shows significant variation with the angle of ejection of the photoelectron. The depth of the delay profile decreases at the location of Cooper minimum as the angle of observation increases till $\theta = 60^0$. At $\theta = 90^0$, the time delay exhibits a positive peak. Apart from this, the confinement induces oscillations in the angle-dependent time delay; the oscillation is more as the charge is migrated to the C_{60} side.

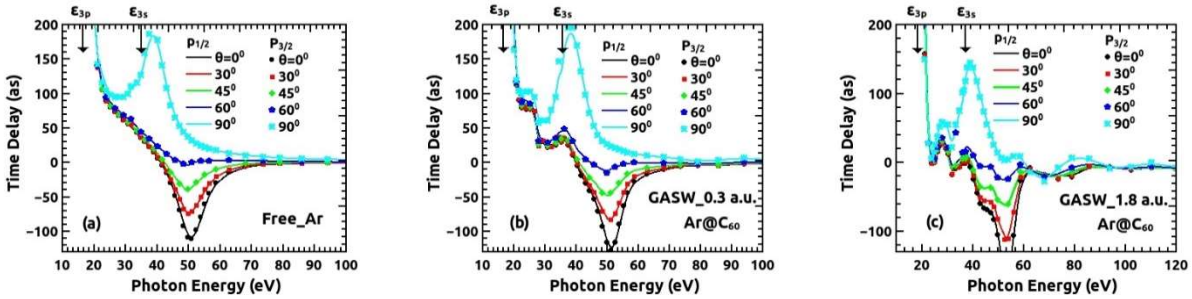

Figure 5. Spin average, angle-dependent time delay of photoionization from the $3p_{1/2}$ and $3p_{3/2}$ subshells of (**a**) free (**left panel**) and confined Ar with the depths of (**b**) 0.3 a.u. (**middle panel**) and (**c**) 1.8 a.u. (**right panel**). Vertical arrows indicate the threshold values of the corresponding subshells used in the RRPA.

The p→εd channel contribution dominates in the entire region except in the Cooper minimum location. At the Cooper minimum, the p→εd matrix element is small and the amplitude of the 'p→εs channel' becomes very competitive with that of the 'p→εd channel'. Thus, a competition between the 'p→εs channel' and 'p→εd channel' makes the time delay sensitive to angle, because the transition amplitude contains the combination of the spherical harmonics terms corresponding to each of the individual dipole matrix elements (see Equation (10)). These spherical harmonics terms lend the information regarding the angle to the spin average time delay $\overline{\tau}$ (see Equations (12)–(14)), which is the weighted average of the individual time delay associated with the individual transition amplitude.

We now try to explain the strange angle dependence of the time delay at the Cooper minimum location; it has already been mentioned that the time delay shows prominent variation with angles at the location of Cooper minimum because of the competition between p→εs and p→εd channels, i.e., among the channels having final states with different orbital angular momenta. The p→εd dominates over the whole energy region except near the Cooper minimum region where both the channels have comparable strength. In fact, p→εs even dominates at the location of Cooper minimum. This competition between channels explains the angular dependence. Special attention is given to the positive time delay at $\theta = 90^\circ$, because a negative time delay is observed at all other angles at the Cooper minimum. One can see that the angle dependence of the time delay in Figure 5 has exactly followed the profile of $\tau_{np_{1/2}}^{m=1/2,+}$ (not shown), which is obtained using the transition amplitude $[T^{1+}]_{np_{1/2}}^{m=\frac{1}{2}}$ in Equation (10c). Therefore, it is sufficient to investigate the angle dependence of the $\tau_{np_{1/2}}^{m=1/2,+}$ obtained using the $[T^{1+}]_{np_{1/2}}^{m=\frac{1}{2}}$. The transition amplitude $[T^{1+}]_{np_{1/2}}^{m=\frac{1}{2}}$ is the linear combination of dipole channels $D_{np_{1/2}\to\varepsilon d_{3/2}}$ and $D_{np_{1/2}\to\varepsilon s_{1/2}}$, weighted using respective spherical harmonics terms Y_{20} and Y_{00}. Since the Y_{00} is isotropic, we do not expect angle dependence to come from it. This means that the angle dependence of the time delay $\tau_{np_{1/2}}^{m=1/2,+}$ is only due to the term Y_{20}. Due to the progressive change of the value, the Y_{20} sign flips at a particular value of theta (θ) between $\theta = 0^\circ$ and $\theta = 90^\circ$. We noticed that the phase shift at the Cooper minimum is decreasing

through $\frac{\pi}{2}$ for angles θ = 0° through θ = 60°, which culminates into negative time delay. For higher angles, due to the sign flip of the Y_{20} the phase shift is increasing through $\frac{\pi}{2}$, which leads to a positive time delay. Thus, the Y_{20} plays the central role in the angle sensitivity of the phase shift and associated time delay at the location of Cooper minimum. In addition to the positive time delay in the vicinity of CM at θ = 90°, another observation is the shift of dip in the time delay to lower energy at θ = 60°. For instance, the dip in the time delay corresponding to the CM occurs at 50.90 eV for θ = 0° and at 48.26 eV for θ = 60° in case of free Ar. Up to a certain angle, θ = 54.73° (magic angle), both the terms $\left(1/\sqrt{15}\right) Y_{20} D_{np_{1/2} \to Ed_{3/2}}$ and $\left(1/\sqrt{6}\right) Y_{00} D_{np_{1/2} \to Es_{1/2}}$ of $[T^{1+}]^{m=\frac{1}{2}}_{np_{1/2}}$ in Equation (10c) have the same sign and follow the similar trend. However, after θ = 54.73°, due to the sign flip of $Y_{20,}$ these two terms of $[T^{1+}]^{m=\frac{1}{2}}_{np_{1/2}}$ have opposite signs and a competition has arisen between them, which leads to the shifting of the location of Cooper minimum towards the lower energy as the photoemission angle increases beyond θ = 54.73°. The aforementioned explanation is presented from a mathematical perspective. From a physical perspective, it is well known that negative and positive time delays correspond to the repulsive and attractive potential. To correlate the shift in time delay from negative to positive as the angle of observation is changed, one can infer that the spherical harmonics present an effective potential (including the centrifugal barrier) that is angle dependent. This happens due to the specific symmetry of the spherical harmonics of the partial waves, which contributes to the anisotropy remarkably.

Note that the above explanation is applicable for both free and confined systems. However, the confinement induces additional oscillations, the degree of which is increasing with charge migration. Confinement oscillations in the time delay are dramatic due to charge migration at depth = 1.8 a.u.

Kr@C_{60}

Photoionization from the *4p* subshell of the Kr@C_{60} is analyzed in this section from the perspective of the charge migration. The choice of the *4p* subshell is motivated by the earlier reports [9] that the subshell exhibits meeker hybridization with the C_{60} subshells. The $4p_{1/2}$ radial wavefunction of the free and confined Kr is shown in Figure 6; the confinement environment is simulated with $V_{GASW}(r_c)$ = 0.3 a.u. and 1.8 a.u. Additionally, Table 2 provides the comparison of the ionization potentials of the *4p* subshells in all cases considered. The table shows that the confinement induces changes in the ionization potentials considerably.

From Figure 6, a weak migration of charge is seen at depth 1.8 a.u. This depth of the model potential is selected by the agreement of the *4p* wavefunction obtained from model confinement with the wavefunction of the complex system calculated from the ab initio LDA theory [9].

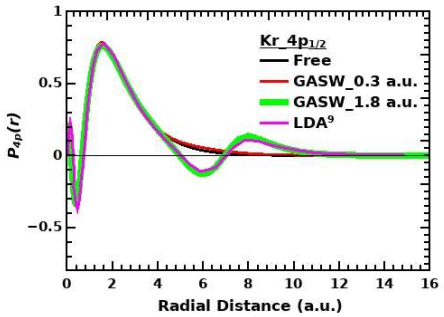

Figure 6. The large component of 4p1/2 radial wavefunction of free and confined Kr.

Table 2. The *4p* subshell thresholds of free and confined Kr.

Depth (a.u.)	Subshells	RRPA (eV)
0 (Free)	4p3/2	13.995
	4p1/2	14.734
0.3	4p3/2	14.715
	4p1/2	15.469
1.8	4p3/2	16.545
	4p1/2	17.237

Additionally, one may note the similarity between the wavefunctions of the free Kr and the Kr@C_{60} with depth = 0.3 a.u. The low confinement depth is insufficient to make any changes to the wave function, but a shift in the threshold is seen.

Figure 7 shows the photoionization cross-sections of the Kr and the Kr @C_{60} for various depths considered in RRPA, compared with the equivalent TDLDA results. Since the threshold for the 4p is shifted in the charge-migrated case, the cross-section has a different onset in the RRPA case shown in Figure 7a. For the free Kr, the cross-sections from TDLDA are in good agreement with the RRPA cross-section. This shows the equivalence of the TDLDA and the RRPA methodologies. The GASW confinement with the depth of 0.3 a.u. does not impact the photoionization cross-section appreciably, which is a similar case as in the Ar@. This is attributed to the low charge migration in this case. On the other hand, the Kr@C_{60} with the $V_{GASW}(r_c)$ = 1.8 a.u. indicates enhanced confinement oscillations, which is a natural ramification of the charge migration. Figure 7b shows the magnified view of the comparison of the RRPA results, which makes clear that the low-depth confinement also induces a feeble oscillation, which is extremely amplified due to the impact of charge migration. Destructive interference in the near-threshold region has brought down the cross-section magnitude for the depth of 1.8 a.u.

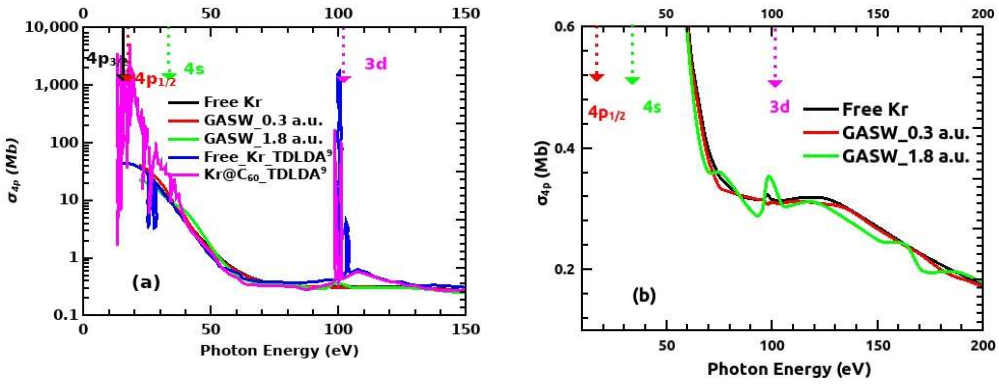

Figure 7. Photoionization cross-sections of the 4p orbital of free and confined Kr using the RRPA are compared with the TDLDA [9] results in (a) (**left panel**). A magnified view of the result is presented in (b) (**right panel**). Vertical arrows indicate the threshold values of the corresponding subshells used in the RRPA.

The free Kr shows a Cooper minimum in the *4p* cross-section at 75 eV. The Cooper minimum region is not strongly affected due to the confinement. However, charge migration does alter the features due to the modulation of the free cross-section with the confinement oscillations. For the confined Kr, the enhancement in cross-section of the TDLDA in the low-photon-energy region mainly arises due to the coupling of atomic photoionization channels with that from the C_{60} shell [9,18,23]. This observation is confirmed as the disparity between the present RRPA with V_{GASW} (r_c) = 1.8 a.u. and the TDLDA is just due to the inclusion of C_{60} photoionization channels. These observations confirm that the decoupling of photoionization channels from the atom@ and the C_{60} electron is made possible. Further,

the information about the degree of alterations in the photoionization parameters due to charge migration alone is also extracted.

In Figure 8, we show the average angular asymmetric parameter β_{4p} of free and Kr@C_{60}. The asymmetry parameter in the free and confined Kr case has a minimum at ~75 eV at the location of Cooper minimum. The free Kr and the Kr@C_{60} with $V_{GASW}(r_c)$ = 0.3 a.u. exhibit similar angular distribution features. However, alterations due to the charge migration are observed at depth 1.8 a.u. A stronger confinement oscillation mediated by the charge migration is quite evident; the oscillations are more prominent within the photon energy range 100 eV to 200 eV because relative phase information of dipole channels is more impacted than dipole amplitude is upon the confinement and charge migration.

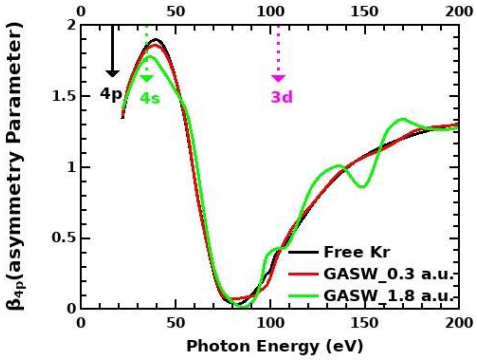

Figure 8. The average angular asymmetric parameter β_{4p} of free and confined Kr. Vertical arrows indicate the threshold values of the corresponding subshells used in the RRPA.

Figure 9 shows the time delay of photoionization of individual channels from the *4p* subshell of free and confined Kr. Left and right axis scales respectively correspond to p→εd and p→εs transition channels. Indication of the Cooper minimum is evident at ~75 eV in the p→εd channel as a sudden negative dip in the time delay. Moreover, the $p\rightarrow\varepsilon s$ channel transition also shows a minimum in time delay at 40 eV. Confinement oscillations are seen for both GASW 0.3 a.u. and 1.8 a.u. cases. In the latter case, the free atom behavior is overdriven by the confinement oscillations. The confinement oscillations are enhanced due to charge migration for a depth of 1.8 a.u. The location of cooper minimum is slightly deviated between different spin–orbit split channels due to the relativistic effects. This effect is less amplified in the Ar, as is expected. The deviation in the Cooper minimum in different channels is more prominent in a confined system. The average 4p time delays are also shown in Figure 9, and are in line with the experimental observations [33]. The explanation for the average time delay is almost similar to that in Ar 3p (Figure 4).

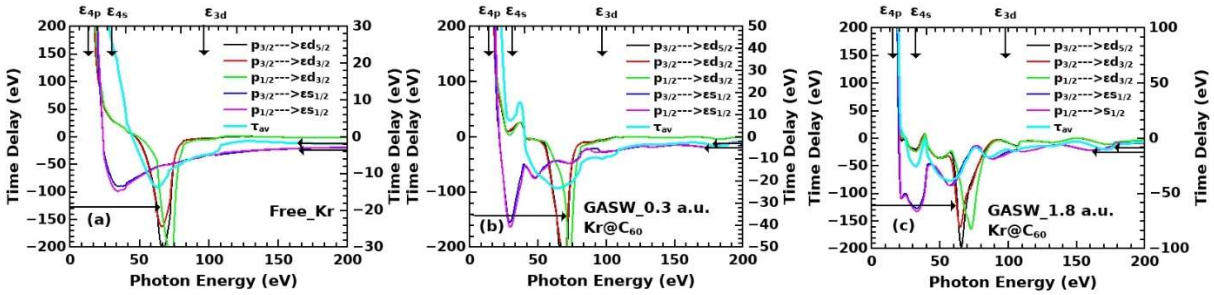

Figure 9. Time delay of photoionization from the 4p subshells of (**a**) free (**left panel**) and confined Kr with the depths of (**b**) 0.3 a.u. (**middle panel**) and (**c**) 1.8 a.u. (**right panel**). Left and right axes are the time scale of the p→εd and p→εs channels, respectively, which are indicated by the horizontal arrows. The average time delay $(\tau_{av})_{4p}$ is also linked to the right axis. Vertical arrows indicate the threshold values of the corresponding subshells used in the RRPA.

One may notice that for the confinement depth of 1.8 a.u., the free atom behavior is almost masked by the confinement effects. For instance, the Cooper minimum features in the time delay are sunk in the pool of confinement features, which makes the atomistic features almost less tractable. The current studies show that the phase shift and the associated properties are largely affected due to the confinement; a stronger impact is seen due to the charge migration.

Figure 10 showcases the impact of charge migration on the angle-dependent, spin-averaged time delay. The figure reasserts that the time delay is very sensitive at the location of Cooper minima to the θ. Time delay in the photoionization from the free atom decreases at the location of Cooper minimum as the angle of observation increases. At 90°, similar to the case of Ar, the time delay exhibits a positive peak in the vicinity of the Cooper minimum location. The comparable magnitude of the dipole transition amplitudes at the Cooper minimum of 4p→εd channel is the reason for dramatic behavior of the angle-dependent time delay at the Cooper minimum. Confinement induces oscillations, which are proportional to the degree of charge migration. In Figure 10c, one can see that the confinement oscillations are driving the free atomistic character of the time delay; for instance, instead of minima, a local maximum is seen for θ = 90° at 75 eV.

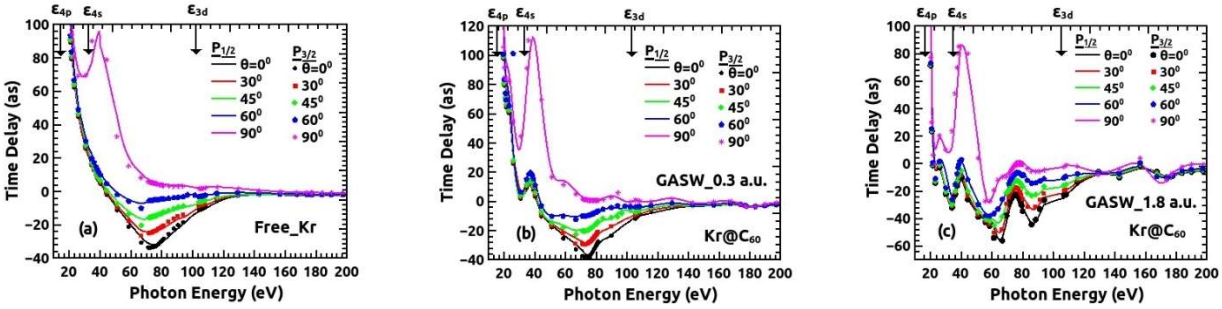

Figure 10. Spin average, angle-dependent time delay of photoionization from the $4p_{1/2}$ and $4p_{3/2}$ subshells of (**a**) free (**left panel**) and confined Kr with the depth of (**b**) 0.3 a.u. (**middle panel**), and (**c**) 1.8 a.u. (**right panel**). Vertical arrows indicate the threshold values of the corresponding subshells used in the RRPA.

$Xe@C_{60}$

It is reported that the *5s* and the *5p* subshells of Xe exhibit a hybridization feature upon entrapment in the C_{60}; hence, these subshells are scrutinized after suitably altering the confinement environment to mimic the charge migration properties akin to the hybridization [18]. The *5s* and $5p_{1/2}$ radial wavefunction of free and confined Xe is shown in Figure 11. Unlike in the case of Kr and Ar, stronger confinement is needed to have a fair agreement with the results of Madjet et al. [18] for both the *5s* and the *5p* subshell densities. The changes in the ionization potentials upon the confinement are compared for different cases in Table 3.

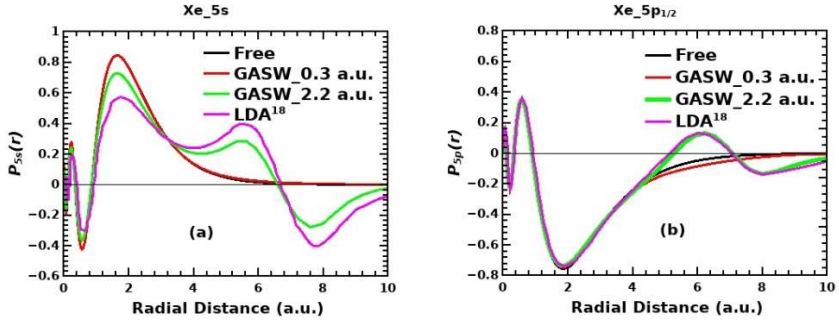

Figure 11. The large component of (**a**) 5s and (**b**) $5p_{1/2}$ radial wavefunctions of free and confined Xe.

Table 3. The 5p and the 5s thresholds of free and confined Xe.

Depth (a.u.)	Subshells	RRPA (eV)
0 (Free)	5p3/2	11.967
	5p1/2	13.401
	5s1/2	27.488
0.3	5p3/2	13.254
	5p1/2	14.734
	5s1/2	28.767
2.2	5p3/2	16.545
	5p1/2	17.237
	5s1/2	33.009

The wavefunctions of Xe@C_{60} *5s* and *5p* subshells are free-atom-like in the case of a confinement depth of 0.3 a.u. When the confinement depth $V_{GASW}(r_c)$ = 2.2 a.u, the *5p* wavefunction exhibits a mixed character of the atomic state and well state. This is accomplished via charge transfer. At this depth, the *5p* wavefunction is in agreement with the ab initio LDA theory [9]. $5p_{3/2}$ and $5p_{1/2}$ wavefunctions are similar in case of $V_{GASW}(r_c)$ = 2.2 a.u. However, the wavefunction obtained from ab initio LDA theory for Xe *5s* wavefunction is qualitatively similar to the wavefunction generated from the GASW model potential for the depth of 2.2 a.u. From Figure 11, we can predict that the model potential can be used successfully to see the effect of hybridization that mimics the charge migration. Figure 11 further shows that the effect of charge migration is comparatively weak for 5*p*, but the 5*s* displays significant charge migration towards the C_{60} orbital. From the hybridization perspective, this type of charge density results if the pairing orbital is a π subshell of the $C_{60,}$ which leads to a node located within the carbon cage [18].

In Figure 12a, the photoionization cross-sections of the *5p* orbital of free and confined Xe are compared with TDLDA [18] results. Similar to the earlier case, the low-depth confinement alters the photoionization cross-section of Xe@C_{60} only a little; on the other hand, the stronger confinement leads to enhanced oscillations. For the confined Xe, the enhancement in cross-section of TDLDA in the low-photon-energy region (C_{60} giant plasmon region) mainly arises due to the coupling of atomic photoionization channels with that from the C_{60}. The cross-section exhibits a Cooper minimum at ~50 eV, which is modulated by the confinement oscillations upon the stronger confinement. There is a second Cooper minimum, which is at relatively higher energies, at ~160 eV. In our calculation, we can study the dynamics after decoupling the impact of C_{60} channels but retaining the hybridization properties. This must be the reason for the discrepancy between the TDLDA result and RRPA with the model potential result for confined Xe in the low-photon-energy region. In the higher energies, qualitatively, the TDLDA and the RRPA agree fairly well, even for some of the confinement resonance features.

The case of *5s* photoionization is much more interesting as the energy region is devoid of plasmon resonances. Hence, we would expect a close comparison and agreement between the TDLDA and the RRPA results; the latter result is anticipated to agree more in the charge-migration-enabled case. In this way, the claim made in the present work can be confirmed unambiguously. Figure 12b shows the photoionization cross-section of the *5s* subshell of the free and confined Xe. These results are compared with LDA and TDLDA results. To have a detailed analysis, the RRPA of Xe@C_{60} with depth = 2.2 a.u. is performed at two levels: (1) a two-channel calculation in which only the channels from the 5s are coupled and (2) a 20-channel calculation in which the channels from $5p_{3/2}$, $5p_{1/2}$, *5s*, $4d_{5/2}$, $4d_{3/2}$, $4p_{3/2}$, $4p_{1/2}$, and *4s* are coupled. The objective behind performing the level 1 calculation is to have a phenomenological agreement between the RRPA and the LDA results. It is known that the two-channel RRPA, which is least correlated, is expected to show a qualitative similarity with the independent particle LDA results. On the other hand, the correlated RRPA calculation does include the effect of interchannel coupling correlation effects, but the discrepancy between the RRPA and the TDLDA is just due to the effect

of the C_{60} channels. In the case of *5s*, since the stronger plasmon coupling is absent, it is anticipated that the RRPA and the TDLDA will show qualitative agreement, at least.

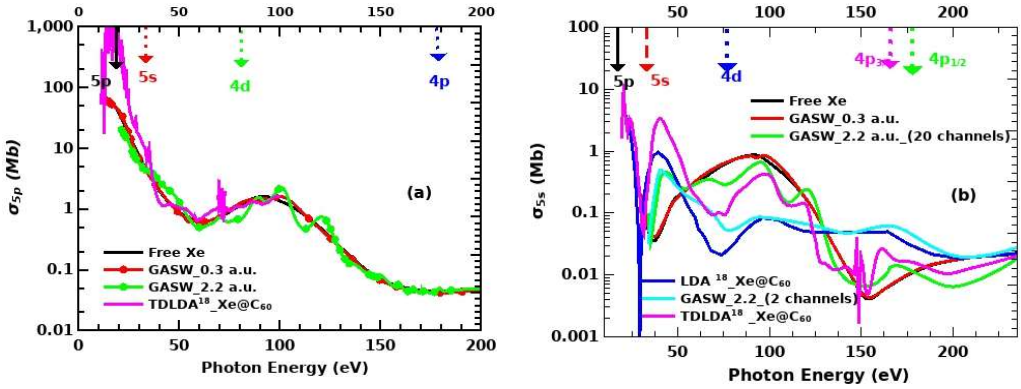

Figure 12. Comparison of photoionization cross-sections of (**a**) 5p (**left panel**) and (**b**) 5s (**right panel**) orbitals of free and confined Xe using the RRPA with LDA [18] and TDLDA [18] results. Vertical arrows indicate the threshold values of the corresponding subshells used in the RRPA.

As expected, the free Xe and the Xe@C_{60} with $V_{GASW}(r_c)$ = 0.3 a.u. do not exhibit stronger alterations, which is partly due to the diminutive charge migration in the confined case. In the case of twenty-channel coupled calculation, the *5s* cross-section amplitude is increased within the energy region between 50 eV and 140 eV due to the coupling between *4d* photoionization channels and those from the *5s* subshells. Two Cooper minima are respectively observed at photon energy 37 eV and 150 eV. The effects of coupling with the *4d* photoionization channels are quite important in the region of both Cooper minima.

The 5s cross-section at depth 2.2 a.u. is significantly impacted due to the confinement and the charge migration; rich confinement resonant features are seen in the 20-channel RRPA results. The comparison with the TDLDA for the *5s* case is quite enriching. It is observed that the *5s*- cross-sections obtained by employing only model potential into the RRPA methodology (20 channels coupled) are in good qualitative and quantitative agreement with the TDLDA cross-sections for confined Xe. The resonant features are similar in both approximations throughout the energy range considered. As expected, the agreement rendered by both models confirms that the charge migration is solely responsible for the oscillations. Since the coupling of channels from the atom with the C_{60} channels is the least expected, the agreement is stronger. Some distortion is seen in the 5s cross-section of the TDLDA calculation within the energy region between 160 eV and 200 eV, which arises due to autoionization resonances of the *4p* subshell.

The comparison of the RRPA calculation in level 1 (2 channels coupled) with the uncorrelated LDA results showcases intriguing agreement. The features in both the cross-sections are similar. From these observations, it has been concluded that charge migration does not dramatically affect the magnitude of cross-section but, of course, impacts the oscillations.

The 5*p* and 5*s* angular distribution asymmetry parameters for free and confined Xe are shown in Figure 13a,b. The β is dependent on the ratio of the magnitudes of the matrix elements of the relativistic dipole channels, along with their relative phases. From Figure 13a, the comparison of 5*p* β of free Xe and Xe@C_{60} for the depth of 2.2 a.u. suggests significant modification due to charge migration in the energy range 50–140 eV. The presence of Cooper minima at ~50 eV and ~160 eV is marked by a minimum in the β_{5p}. Since there are two Cooper minima in the 5p$\rightarrow$*d* channels, the contribution to the cross-section is predominantly by the 5p$\rightarrow$*s* channels. One may note that the β_{5p} at the Cooper minima locations is close to zero, which ensures an isotropic angular distribution of the photoionization cross-section at the Cooper minimum location. One may note the shift in the Cooper minima features in the confined case. The shifting of the location of

the Cooper minimum in the β_{5p} profile for confined Xe at depth of 2.2 a.u. is primarily due to the confinement oscillations due to the charge migration altering the free atom characteristics.

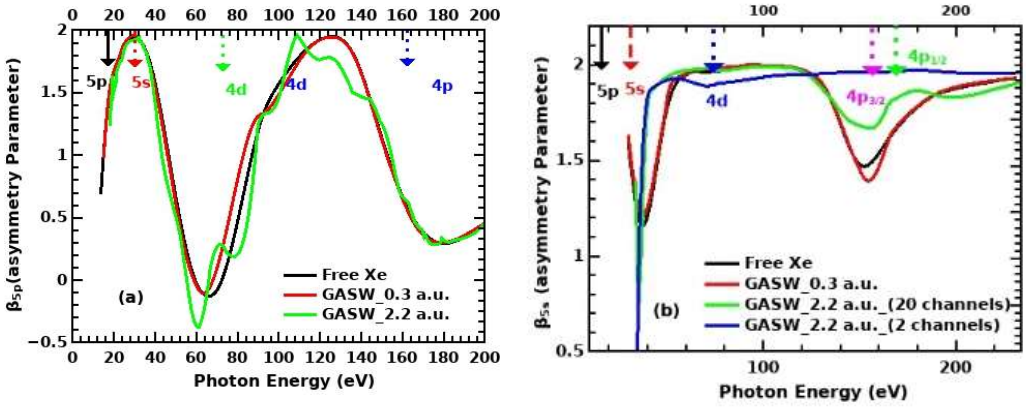

Figure 13. The average angular asymmetric parameter of free and Xe@C_{60} for (**a**) 5p and (**b**) 5s orbitals. Vertical arrows indicate the threshold values of the corresponding subshells used in the RRPA.

In the case of twenty-channel coupled calculation, the β_{5s} deviates from two due to the effects of Cooper minimum at 37 eV and 150 eV (Figure 13b). It is a well-known fact that the β_{ns} deviates from its nonrelativistic value—two—when the relativistic effects are dominant. The Cooper minimum is a sensitive indicator of correlation and relativistic effects. For instance, the second Cooper minimum is absent in the case of the two-channel coupled calculation, which is indicated by the flat value of β_{5s} at ~160 eV. This makes evident that the second Cooper minimum results from the final state correlation effects. On top of the relativistic and correlation effects, the stronger confinement induces oscillations in the β profile also.

In Figure 14, the two Cooper minima are indicated in the individual channel time delay of photoionization from the *5p* subshell of free and confined Xe by a dip with large negative value. For free and confined Xe, the cooper minima are seen in the $5p \rightarrow \varepsilon d$ channel at about 50 eV and 160 eV. Confinement oscillations are observed, as expected. It has been enhanced for the case of depth = 2.2 a.u. due to the charge migration. In the case of depth of 2.2 a.u., the cooper minimum features in the time delay are hidden in the dramatic confinement oscillations. The amplitude of confinement oscillations in the time delay profile is increased within the energy region between 80 eV and 140 eV due to the interchannel coupling with the 5s channels, which is cascaded through the coupling of *4d* ionization channels. The explanation for the average time delay $(\tau_{av})_{5p}$ is analogous to that in Ar 3p and Kr 5p (Figures 4 and 9).

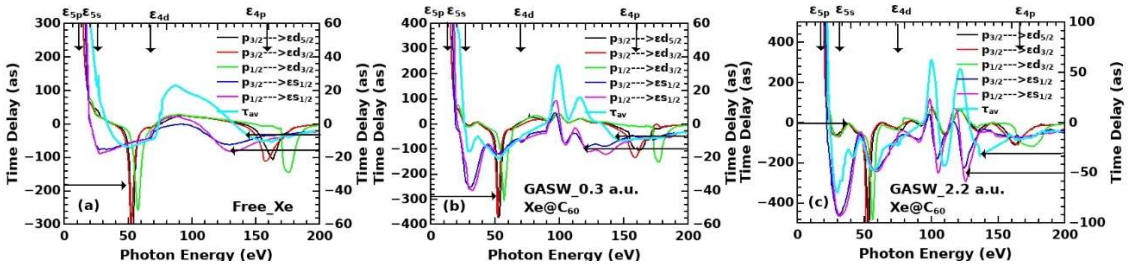

Figure 14. Time delay of photoionization from the 5p subshell of (**a**) free and confined Xe using the depths of (**b**) 0.3 a.u. (**middle panel**) and (**c**) 2.2 a.u. (**right panel**). Left and right axes are the time scale of the p→εd and p→εs channels, respectively, which are indicated by the horizontal arrows. The average time delay $(\tau_{av})_{5p}$ is also linked to the right axis. Vertical arrows indicate the threshold values of the corresponding subshells used in the RRPA.

In Figure 15, two Cooper minima features are observed in the individual channel time delay of photoionization from the 5s subshell for free and confined Xe. For free and Xe@C_{60} using $V_{GASW}(r_c)$ = 0.3 a.u., the cooper minima are seen at 37 eV and 160 eV. However, the first Cooper minimum is barely visible for the case of depth = 2.2 a.u. as a small shoulder at ~37 eV. This means that the stronger confinement oscillations in the Xe@C_{60} overdrive the atomistic features, mediated through the charge migration. The second minimum is evident as a dip in the time delay at 150 eV. However, the features are sunk in the sea of oscillations due to confinement and charge migration. The location of cooper minimum has slightly deviated between $5s_{1/2}\rightarrow\varepsilon p_{3/2}$ and $5s_{1/2}\rightarrow\varepsilon p_{1/2}$ channels due to the large relativistic effects. Specifically, the $5s_{1/2}\rightarrow\varepsilon p_{1/2}$ minimum occurs at lower energy than that of the $5s_{1/2}\rightarrow\varepsilon p_{3/2}$, because the spin–orbit force is attractive for $p_{1/2}$ and repulsive for $p_{3/2}$. The amplitude of confinement oscillations in the time delay profile is increased within the energy region between 80 eV and 140 eV due to interchannel coupling in the 4d photoionization channels of Xe on *5s* photoionization amplitude.

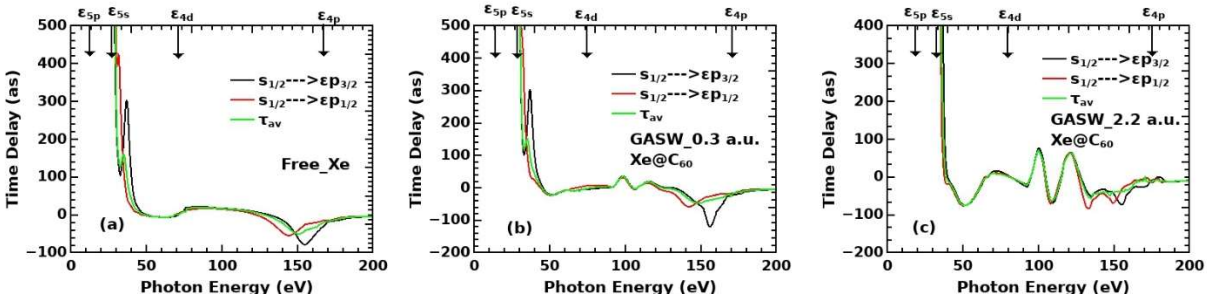

Figure 15. Time delay of photoionization from the 5s subshell of (**a**) free and confined Xe using the depths of (**b**) 0.3 a.u. (**middle panel**) and (**c**) 2.2 a.u. (**right panel**). Vertical arrows indicate the threshold values of the corresponding subshells used in the RRPA.

Figure 16 shows the spin average, angle-dependent time delay of 5p free and confined Xe. Angle-dependent time delay is sensitive to the Cooper minimum location. The oscillations in the time delay are enhanced as the depth increases. The explanation for the strange angle dependence of the time delay is almost similar to that in Ar 3p (Figure 5) and Kr 4p (Figure 10). The Y_{20} controls the phase shift at the Cooper minimum and therefore the sign of the time delay is also flipped. However, the relativistic effect is more prominent for Xe compared to Ar and Kr. Due to the relativistic effect, a small difference occurs in the spin-averaged time delay profile of Xe $5p_{1/2}$ and $5p_{3/2}$; the difference is evident for $\theta = 90^0$.

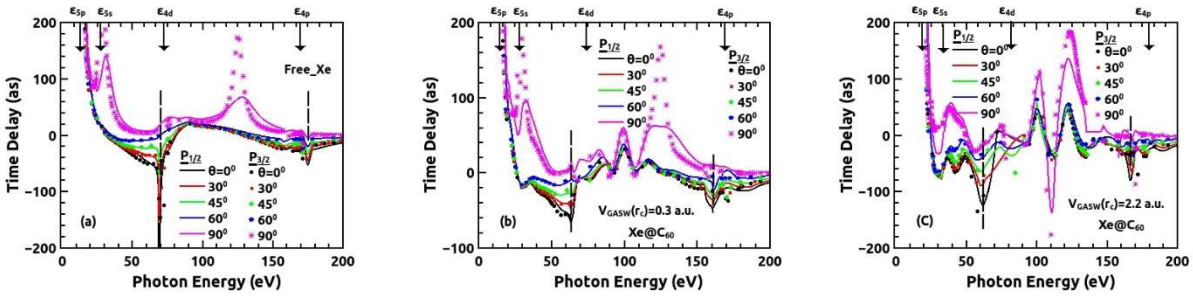

Figure 16. Spin average, angle-dependent time delay of photoionization from the 5p subshell of (**a**) free and confined Xe using the depths of (**b**) 0.3 a.u. (**middle panel**) and (**c**) 2.2 a.u. (**right panel**). Vertical lines denote the location of Cooper minima. Vertical arrows indicate the threshold values of the corresponding subshells used in the RRPA.

Figure 17 shows the spin average, angle-dependent time delay of 5s free and confined Xe. Two Cooper minima regions are respectively observed at photon energy 37 eV and 150 eV. Angle-dependent time delay is very sensitive at the location of Cooper minima

for free Xe and confined Xe. We attempt to explain the features of angular dependence of the time delay in the 5s case. The time delays are almost the same for θ = 0° to 60°, but completely different at 90°. According to Equation (12), the spin average time delays are weighted by the absolute squares of the respective $[T_{10}^{1\pm}]_{ns_{1/2}}^{m=\frac{1}{2}}$ amplitudes. However, for the angles θ = 0° to 60°, the angle-dependent time delay exactly follows the spin-up time delays $\left(\tau_{ns_{1/2}}^{m=\frac{1}{2},+}\right)$ associated with transition amplitude $[T_{10}^{1+}]_{ns_{1/2}}^{m=\frac{1}{2}}$, and at 90°, it follows the spin-down time delays $\left(\tau_{ns_{1/2}}^{m=\frac{1}{2},-}\right)$. It is clear from Equation (10) that the absolute square of $[T_{10}^{1+}]_{ns_{1/2}}^{m=\frac{1}{2}}$ depends upon $\cos^2\theta$, while the absolute square of $[T_{10}^{1-}]_{ns_{1/2}}^{m=\frac{1}{2}}$ depends on $\sin^2\theta$. Thus, for θ = 0^0, the spin-down contribution vanishes, and the spin average, angle-dependent time delays are exactly the same as the spin-up time delays, while at θ = 90^0, the spin-up contribution vanishes, and the spin-averaged angle-dependent time delays must follow the spin-down time delays [48].

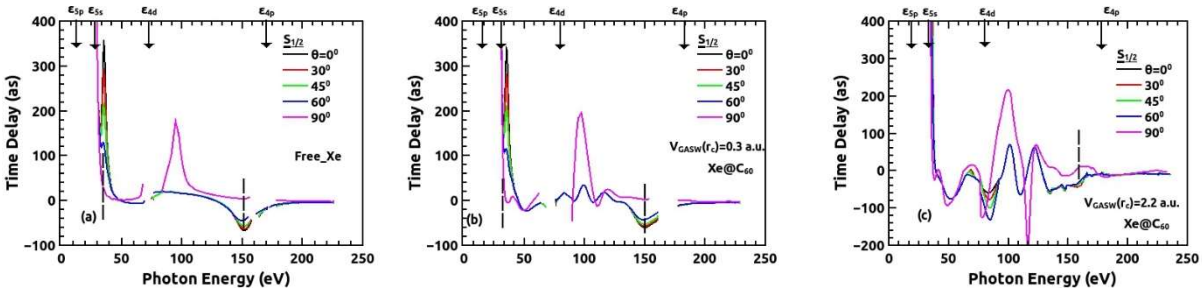

Figure 17. Spin average, angle-dependent time delay of photoionization from the 5s subshell of (**a**) free and confined Xe using the depths of (**b**) 0.3 a.u. (**middle panel**) and (**c**) 2.2 a.u. (**right panel**). Vertical lines denote the location of Cooper minima. Vertical arrows indicate the threshold values of the corresponding subshells used in the RRPA.

Cooper minima features are not distinguishable in the time delay for the depth 2.2 a.u. In other words, the Cooper minimum features in the time delay are lost in the confinement oscillations. Similar behavior is seen in the case of cross-section also.

4. Conclusions

The long-standing question regarding the effect of charge migration on the photoionization from the X@C_{60} is investigated in the present work. The correlated calculations employing the sophisticated RRPA methodology ensure a sufficient amount of relativistic and correlation effects. Three noble gas atoms, Ar, Kr, and Xe, are entrapped in the C_{60} and investigated for the effect of charge migration on the photoionization parameters. The effect of charge migration is akin to the hybridization, which in turn is controlled by the size of the atom. Since the expansion of the radial wavefunctions depends on the size of the atom, we can expect that the coupling of the outer orbitals of Xe with the C_{60} orbitals is relatively more compared to Ar. Hence, we expect that Xe is more susceptible to changes.

A systematic comparison of the results from the present studies with the TDLDA results deciphers that the coupling of atomic and C_{60} photoionization channels leads to enhancement in the cross-section. However, the present work shows a qualitative comparison with LDA and TDLDA results, and the impact of the charge migration is only in producing the enhanced confinement oscillations. Moreover, the confinement oscillations are more evident on the angular distribution asymmetry parameter and the time delay than on the cross-section. This is due to the enhanced sensitivity of dipole phase shift on the confinement. Few striking features are observed in the angle-resolved, spin average time delay at the Cooper minimum. The location of the dip in the angular time delay at the Cooper minimum is shifted towards the lower photon energy for the

photoemission angle beyond θ = 54.73°. Further, a positive time delay at Cooper minimum occurs at θ = 90° for *np* subshells. In case of *ns* subshells, the dip in the time delay at the Cooper minimum location is also angle sensitive. For the angles θ = 0° to 60°, the spin-average, angle-dependent time delay is following the spin-up time delays $\left(\tau_{ns_{1/2}}^{m=\frac{1}{2},+}\right)$ associated with transition amplitude $[T_{10}^{1+}]_{ns_{1/2}}^{m=\frac{1}{2}}$, and at 90°, it is following the spin-down time delays $\left(\tau_{ns_{1/2}}^{m=\frac{1}{2},-}\right)$ associated with transition amplitude $[T_{10}^{1-}]_{ns_{1/2}}^{m=\frac{1}{2}}$. Moreover, the angle average (τ_{av}) and spin average, angle-resolved time delays in photoionization are possible to measure experimentally; these quantities can be compared in search of the realistic potentials in the context of charge migration.

The angular distribution asymmetry parameter has also shown remarkable connection to the charge migration. However, the present study only included the dipole effects. It is well known that the location of dipole Cooper minimum, the impact of non-dipole terms could be of significance [49,50]. For instance, in Mg 3s and Ca 4s, it has been shown theoretically that the dipole–quadrupole and quadrupole–quadrupole interference terms contribute to the angular distribution asymmetry especially at the location of dipole Cooper minimum [51,52]. Therefore, the time delay can also be impacted by the non-dipole channels at the location of dipole Cooper minimum. Nevertheless, because of the enhanced spin–orbit splitting in heavier elements, the Cooper minimum in dipole channels from the spin–orbit split channels is not coincided and hence the non-dipole effects will still be suppressed. Therefore, the impact of non-dipole effects is more prominent for low-Z atoms. However, a future work in the direction to isolate the impact of charge migration on the non-dipole angular distribution asymmetry parameter will be worthwhile.

This is the first work in which the decoupling of C_{60} channels and hybridization is made possible. In this regard, we vary the depth of the GASW potential to simulate identical electronic charge density as in the case of a realistic X@C_{60}. The model potential approach cannot mimic the hybridization properties since there is a limitation in taking into account the electron correlation of the C_{60} channels. However, the present methods are capable of making realistic predictions when the coupling effects from the C_{60} channels are unimportant. For example, the 5s photoionization results from the Xe@C_{60} will be potential candidates to verify the conclusions drawn from the present work, as in the particular region, the plasmon resonance is very weak. Hence, the present conclusions can trigger experiments to validate the predictions regarding the impact of charge migration.

Author Contributions: S.S., S.B., J.J.: investigation, formal analysis, and writing—review and editing; S.S.: investigation; S.S., J.J., S.B.: writing—original draft preparation and editing; S.S., J.J.: methodology and supervision; S.S., J.J.: review and resources; S.S., S.B., J.J.: conceptualization, software, review, and validation. All authors have read and agreed to the published version of the manuscript.

Funding: J.J. acknowledges the support provided by SERB through Project No. ECR/2016/001564.

Data Availability Statement: The data generated part of this study are all used and are available in this manuscript.

Acknowledgments: The authors are grateful to P. C. Deshmukh for helpful discussions.

Conflicts of Interest: The authors declare no conflict of interest.

References

1. Connerade, J.; Dolmatov, V.; Manson, S. On the nature and origin of confinement resonances. *J. Phys. B At. Mol. Opt. Phys.* **2000**, *33*, 2279. [CrossRef]
2. Chakraborty, H.S.; Madjet, M.E.; Rost, J.-M.; Manson, S.T. Dynamical effects of confinement on atomic valence photoionization in Mg@C_{60}. *Phys. Rev. A* **2008**, *78*, 013201. [CrossRef]
3. Dolmatov, V.K.; Baltenkov, A.S.; Connerade, J.P.; Manson, S.T. Structure and photoionization of confined atoms. *Radiat. Phys. Chem.* **2004**, *70*, 417–433. [CrossRef]

4. Connerade, J.; Dolmatov, V.; Pochincherla, A.L.; Manson, S. Electron structure of endohedrally confined atoms: Atomic hydrogen in an attractive shell. *J. Phys. B At. Mol. Opt. Phys.* **1999**, *32*, L239. [CrossRef]
5. Amusia, M.Y.; Chernysheva, L.V.; Dolmatov, V.K. Confinement and correlation effects in the Xe@C_{60} generalized oscillator strengths. *Phys. Rev. A* **2011**, *84*, 063201. [CrossRef]
6. Kilcoyne, A.L.D.; Aguilar, A.; Müller, A.; Schippers, S.; Cisneros, C.; Alna'Washi, G.; Aryal, N.B.; Baral, K.K.; Esteves, D.A.; Thomas, C.M.; et al. Confinement Resonances in Photoionization of Xe@C_{60}^+. *Phys. Rev. Lett.* **2010**, *105*, 213001. [CrossRef]
7. Thuppilakkadan, A.; Jose, J.; Varma, H.R. Systematic study of Coulomb confinement resonances of atoms trapped inside charged fullerenes. *Phys. Rev. A* **2020**, *102*, 062826. [CrossRef]
8. Chakraborty, H.S.; Madjet, M.E.; Renger, T.; Rost, J.-M.; Manson, S.T. Photoionization of hybrid states in endohedral fullerenes. *Phys. Rev. A* **2009**, *79*, 061201. [CrossRef]
9. Javani, M.H.; Chakraborty, H.; Manson, S. Valence photoionization of noble-gas atoms confined in the fullerene C60. *Phys. Rev. A* **2014**, *89*, 053402. [CrossRef]
10. Altick, P.L.; Glassgold, A.E. Correlation Effects in Atomic Structure Using the Random-Phase Approximation. *Phys. Rev.* **1964**, *133*, A632–A646. [CrossRef]
11. Grant, I.P. *Relativistic Quantum Theory of Atoms and Molecules: Theory and Computation*; Springer: New York, NY, USA, 2007.
12. Johnson, W.R.; Lin, C.D. Multichannel relativistic random-phase approximation for the photoionization of atoms. *Phys. Rev. A* **1979**, *20*, 964–977. [CrossRef]
13. Johnson, W.R.; Lin, C.D.; Cheng, K.T.; Lee, C.M. Relativistic Random-Phase Approximation. *Phys. Scr.* **1980**, *21*, 409–422. [CrossRef]
14. Kelly, H.P. Many-Body Perturbation Theory Applied to Atoms. *Phys. Rev.* **1964**, *136*, B896–B912. [CrossRef]
15. Radojević, V.; Johnson, W.R. Multiconfiguration Tamm-Dancoff approximation applied to photoionization of the outer shells of Be and Mg. *Phys. Rev. A* **1985**, *31*, 2991–2994. [CrossRef]
16. Tong, X.M.; Lin, C.D. Empirical formula for static field ionization rates of atoms and molecules by lasers in the barrier-suppression regime. *J. Phys. B At. Mol. Opt. Phys.* **2005**, *38*, 2593–2600. [CrossRef]
17. Zhang, Q.; Lan, P.; Lu, P. Empirical formula for over-barrier strong-field ionization. *Phys. Rev. A* **2014**, *90*, 043410. [CrossRef]
18. Madjet, M.E.; Renger, T.; Hopper, D.E.; McCune, M.A.; Chakraborty, H.S.; Rost, J.-M.; Manson, S.T. Photoionization of Xe inside C_{60}: Atom-fullerene hybridization, giant cross-section enhancement, and correlation confinement resonances. *Phys. Rev. A* **2010**, *81*, 013202. [CrossRef]
19. Puska, M.J.; Nieminen, R.M. Photoabsorption of atoms inside C_{60}. *Phys. Rev. A* **1993**, *47*, 1181–1186. [CrossRef]
20. Saha, S.; Thuppilakkadan, A.; Varma, H.R.; Jose, J. Photoionization dynamics of endohedrally confined atomic H and Ar: A contrasting study between compact versus diffused model potential. *J. Phys. B At. Mol. Opt. Phys.* **2019**, *52*, 145001. [CrossRef]
21. Wendin, G.; Wästberg, B. Many-electron effects in BaC_{60}: Collective response and molecular effects in optical conductivity and photoionization. *Phys. Rev. B* **1993**, *48*, 14764–14767. [CrossRef]
22. Shields, D.; De, R.; Madjet, M.; Manson, S.; Chakraborty, H. Photoemission from Hybrid States of Cl@C_{60} before and after a Stabilizing Charge Transfer. *J. Phys. B. At. Mol. Opt. Phys.* **2019**, *53*, 125101. [CrossRef]
23. Madjet, M.E.; Chakraborty, H.S.; Manson, S.T. Giant Enhancement in Low Energy Photoemission of Ar Confined in C_{60}. *Phys. Rev. Lett.* **2007**, *99*, 243003. [CrossRef] [PubMed]
24. Deshmukh, P.C.; Mandal, A.; Saha, S.; Kheifets, A.S.; Dolmatov, V.K.; Manson, S.T. Attosecond time delay in the photoionization of endohedral atoms *A*@C_{60}: A probe of confinement resonances. *Phys. Rev. A* **2014**, *89*, 053424. [CrossRef]
25. Johnson, W.R.; Lin, C.D. Relativistic random phase approximation applied to atoms of the He isoelectronic sequence. *Phys. Rev. A* **1976**, *14*, 565–575. [CrossRef]
26. Kumar, S.S.; Banerjee, T.; Deshmukh, P.C.; Manson, S.T. Spin-orbit-interaction activated interchannel coupling in dipole and quadrupole photoionization. *Phys. Rev. A* **2009**, *79*, 043401. [CrossRef]
27. Mandal, A.; Deshmukh, P.C.; Kheifets, A.S.; Dolmatov, V.K.; Manson, S.T. Angle-resolved Wigner time delay in atomic photoionization: The 4*d* subshell of free and confined Xe. *Phys. Rev. A* **2017**, *96*, 053407. [CrossRef]
28. Thuppilakkadan, A.; Jose, J.; Varma, H.R. Photoionization dynamics of Ar trapped in a fullerene anion: Coulomb confinement resonances in 2s subshell and its impact on the 3s subshell. *Phys. Scr.* **2021**, *96*, 104004. [CrossRef]
29. Wigner, E.P. Lower Limit for the Energy Derivative of the Scattering Phase Shift. *Phys. Rev.* **1955**, *98*, 145–147. [CrossRef]
30. Kheifets, A.; Mandal, A.; Deshmukh, P.C.; Dolmatov, V.K.; Keating, D.A.; Manson, S.T. Relativistic calculations of angle-dependent photoemission time delay. *Phys. Rev. A* **2016**, *94*, 013423. [CrossRef]
31. Saha, S.; Mandal, A.; Jose, J.; Varma, H.R.; Deshmukh, P.C.; Kheifets, A.S.; Dolmatov, V.K.; Manson, S.T. Relativistic effects in photoionization time delay near the Cooper minimum of noble-gas atoms. *Phys. Rev. A* **2014**, *90*, 053406. [CrossRef]
32. Klünder, K.; Dahlström, J.M.; Gisselbrecht, M.; Fordell, T.; Swoboda, M.; Guénot, D.; Johnsson, P.; Caillat, J.; Mauritsson, J.; Maquet, A.; et al. Probing Single-Photon Ionization on the Attosecond Time Scale. *Phys. Rev. Lett.* **2011**, *106*, 143002. [CrossRef] [PubMed]
33. Palatchi, C.; Dahlström, J.M.; Kheifets, A.S.; Ivanov, I.A.; Canaday, D.M.; Agostini, P.; DiMauro, L.F. Atomic delay in helium, neon, argon and krypton. *J. Phys. B At. Mol. Opt. Phys.* **2014**, *47*, 245003. [CrossRef]
34. Houlgate, R.G.; Codling, K.; Marr, G.V.; West, J.B. Angular distribution and photoionization cross section measurements on the 3p and 3s subshells of argon. *J. Phys. B At. Mol. Phys.* **1974**, *7*, L470–L473. [CrossRef]

35. Johnson, W.R.; Cheng, K.T. Photoionization of the outer shells of neon, argon, krypton, and xenon using the relativistic random-phase approximation. *Phys. Rev. A* **1979**, *20*, 978–988. [CrossRef]
36. Keating, D.A.; Manson, S.T.; Dolmatov, V.K.; Mandal, A.; Deshmukh, P.C.; Naseem, F.; Kheifets, A.S. Intershell-correlation-induced time delay in atomic photoionization. *Phys. Rev. A* **2018**, *98*, 013420. [CrossRef]
37. Baltenkov, A.; Manson, S.; Msezane, A.Z. Jellium model potentials for the C60 molecule and the photoionization of endohedral atoms, A@C_{60}. *J. Phys. B At. Mol. Opt. Phys.* **2015**, *48*, 185103. [CrossRef]
38. Martínez-Flores, C.; Cabrera-Trujillo, R. Dipole and generalized oscillator strength derived electronic properties of an endohedral hydrogen atom embedded in a Debye-Hückel plasma. *Matter Radiat. Extrem.* **2018**, *3*, 227–242. [CrossRef]
39. Gorczyca, T.W.; Hasoglu, M.F.; Manson, S.T. Photoionization of endohedral atoms using *R*-matrix methods: Application to Xe@C_{60}. *Phys. Rev. A* **2012**, *86*, 033204. [CrossRef]
40. Connerade, J.P.; Dolmatov, V.K.; Manson, S.T. A unique situation for an endohedral metallofullerene. *J. Phys. B At. Mol. Opt. Phys.* **1999**, *32*, L395–L403. [CrossRef]
41. Varma, H.R.; Deshmukh, P.C.; Dolmatov, V.K.; Manson, S.T. Correlation and relativistic effects on the photoionization of confined atoms. *Phys. Rev. A* **2007**, *76*, 012711. [CrossRef]
42. Winstead, C.; McKoy, V. Elastic electron scattering by fullerene, C_{60}. *Phys. Rev. A* **2006**, *73*, 012711. [CrossRef]
43. Dolmatov, V.K.; Amusia, M.Y.; Chernysheva, L.V. Electron elastic scattering off *A*@C_{60}. The role of atomic polarization under confinement. *Phys. Rev. A* **2015**, *92*, 042709. [CrossRef]
44. Saha, S.; Thuppilakkadan, A.; Varma, H.R.; Jose, J. Photoionization phase shift and Wigner time delay of endohedrally confined atoms using transient phase methods. *Eur. Phys. J. Plus* **2020**, *135*, 753. [CrossRef]
45. Jose, J.; Pradhan, G.B.; Radojević, V.; Manson, S.T.; Deshmukh, P.C. Electron correlation effects near the photoionization threshold: The Ar isoelectronic sequence. *J. Phys. B At. Mol. Opt. Phys.* **2011**, *44*, 195008. [CrossRef]
46. Jose, J.; Pradhan, G.B.; Radojević, V.; Manson, S.T.; Deshmukh, P.C. Dipole and quadrupole photodetachment/photoionization studies of the Ar isoelectronic sequence. *J. Phys. Conf. Ser.* **2012**, *388*, 022098. [CrossRef]
47. Jose, J.; Pradhan, G.B.; Radojević, V.; Manson, S.T.; Deshmukh, P.C. Valence photodetachment of Li^- and Na^- using relativistic many-body techniques. *Phys. Rev. A* **2011**, *83*, 053419. [CrossRef]
48. Ganesan, A.; Banerjee, S.; Deshmukh, P.C.; Manson, S.T. Photoionization of Xe 5s: Angular distribution and Wigner time delay in the vicinity of the second Cooper minimum. *J. Phys. B At. Mol. Opt. Phys.* **2020**, *53*, 225206. [CrossRef]
49. Derevianko, A.; Johnson, W.; Cheng, K. Non-dipole effects in photoelectron angular distributions for rare gas atoms. *At. Data Nucl. Data Tables* **1999**, *73*, 153–211. [CrossRef]
50. Ilchen, M.; Hartmann, G.; Gryzlova, E.V.; Achner, A.; Allaria, E.; Beckmann, A.; Braune, M.; Buck, J.; Callegari, C.; Coffee, R.N.; et al. Symmetry breakdown of electron emission in extreme ultraviolet photoionization of argon. *Nat. Commun.* **2018**, *9*, 4659. [CrossRef]
51. Kumar, A.; Varma, H.R.; Pradhan, G.B.; Deshmukh, P.C.; Manson, S.T. Photoionization of Ca 4s in a spherical attractive well potential: Dipole, quadrupole and relativistic effects. *J. Phys. B At. Mol. Opt. Phys.* **2014**, *47*, 185003. [CrossRef]
52. Pradhan, G.B.; Jose, J.; Deshmukh, P.C.; LaJohn, L.A.; Pratt, R.H.; Manson, S.T. Cooper minima: A window on nondipole photoionization at low energy. *J. Phys. B At. Mol. Opt. Phys.* **2011**, *44*, 201001. [CrossRef]